Università degli Studi di Napoli Federico II

Dipartimento di Ingegneria Elettrica e Tecnologie dell'Informazione

Analysis and Control of 1-DOF roll dynamics of a ship with active fins

Project of Nonlinear Dynamics and Control course

Mario Valentino
P38000205

July 2024

Contents

List of Figures

List of Tables

This report has been enhanced with the assistance of ChatGPT to identify and correct spelling and grammatical errors and to improve the overall quality of the English language used.

Chapter 1

Introduction

In this chapter, we will motivate the importance of stabilizing the roll motion of a ship in rough seas, and we will briefly discuss some solutions used nowadays in industry. Afterwards, we will derive a state space model to represent the ship's dynamics, focusing on a simplified 1-DOF model for roll motion. The model will incorporate various forces acting on the ship, such as hydrodynamic moments and control moments from fin actuation.

1.1 Motivations

The ability to control a ship's tendency to roll in response to waves is crucial for ensuring safety on cargo ships and comfort on passenger ships. The movement of cargo on ships can be hazardous, especially in rough seas. Unsecured cargo can shift, causing damage to itself or other cargo, and pose a safety risk to crew members. Rough seas can also cause significant discomfort for passengers, particularly those prone to motion sickness or seasickness.

Various technologies have been employed to address this issue. Bilge keels are built on the hull to increase the hydrodynamic resistance to roll motion. Another basic but effective solution is the use of passive anti-roll tanks, which are U-shaped tanks filled with liquid that dampen the ship's roll motion. When passive solutions are insufficient, active systems can be utilized. Active anti-roll tanks have pumps that force liquid flow from one side to another, producing a restoring force in the desired direction.

Currently, active fins are recognized as the most efficient solution in the industry. These fins, mounted on the hull, change their angle of attack to generate a torque that compensates for the torque induced by the waves. This project focuses on the analysis and control of such active stabilizers.

Although this solution is widely used in the industry, it loses effectiveness when the

vessel is at rest. Significant efforts are being invested in designing control systems for active fins that can stabilize vessels when not underway, such as the Rolls Royce Stabilization At Rest technology [1].

1.2 Mathematical model

The dynamics of a generic rigid body can be represented by a 6-DOF state space model. The degrees of freedom of the vessel are given by *surge, sway, heave, roll, pitch* and *yaw* motions, as illustrated in Figure 1.1. Regarding the problem of controlling the rolling dynamics with active fins, a simplified model can be utilized. In particular, if the fins are positioned longitudinally before or after the vessel's center of gravity, they will induce a yaw motion, necessitating a model with at least 4-DOF. However, constructors usually take into account this effect and place the fins sufficiently close to the center of gravity, reducing the coupling between yaw and roll motions due to fin actuation, thus justifying the use of a 1-DOF model [2].

The derivation of the model is not at the center of this project work. Nevertheless, basic aspects of the model are presented, as they offer valuable insights for the subsequent analysis and control phases.

The 1-DOF model can be written as it follows:

$$\begin{cases} \dot{\phi} = p \\ I_x \dot{p} = M_h + M_c + M_d \end{cases} \tag{1.1}$$

where the symbols in Equation 1.1 represent:

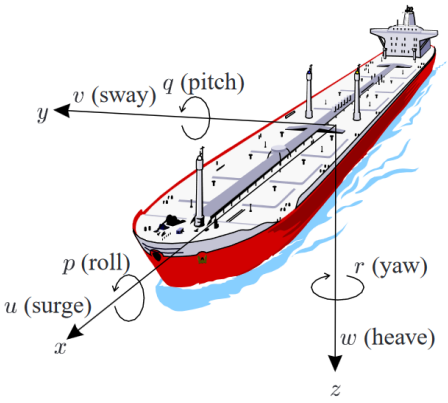

Figure 1.1: Definition of the six degrees of freedom of a vessel [3]

- ϕ : roll angle;
- p : roll rate;
- I_x : moment of inertia;
- M_h : hydrodynamic moment;
- M_c : control moment due to fins actuation;
- M_d : disturbance moment given by the waves, it will be considered later.

Although different representations can be used for hydrodynamic moments and the control moments, in this work we will use the forms given in [4]. The vessel is considered at constant forward speed $U > 0$, and the hydrodynamic moment is decomposed in two contributions: the moment M_{h0} given by the vessel at rest, and the moment M_{hU} given by the surge speed. In particular:

$$M_{h0} = K_{\dot{p}}\dot{p} + K_p p + K_{p|p|}p|p| - M(\phi) \tag{1.2}$$

$$M_{hU} = K_{Up}Up + K_{\phi UU}U^2\phi \tag{1.3}$$

$M(\phi)$ is the righting moment that restores the vessel back to its equilibrium attitude when perturbed.

$$M(\phi) = K_\phi \sin(\phi) \tag{1.4}$$

The coefficients in Equations 1.2-1.4, are identified using experimental approaches. In this work, we will use the same parameters used by [2] that are listed in Table 1.1.

Concerning the control moment, the authors in [2] used an approximated expression given by:

$$M_c = -2\frac{K_\alpha r_f}{U} - 2K_\alpha \alpha \tag{1.5}$$

This expression shows that the fins produce a damping moment due to their extension in the water, and a lift moment generated by their mechanical angle α, which is the actual control input . K_α is a parameter that increases with the forward speed, density of water, area of each fin and lift coefficient. r_f is the arm between the lift forces acting on the fins and the center of gravity of the vessel. This approximated expression of the control moment is valid when cruising at a forward speed that is sufficiently large to generate lift. Furthermore, the moment increases linearly with the mechanical angle until the stall angle is reached. A saturation in the control action must be added to avoid this operating condition.

The complete model of the vessel roll can be rewritten as:

$$\begin{cases} \dot{\phi} = p \\ (I_X - K_{\dot{p}})\dot{p} = (K_p + K_{Up}U - 2\dfrac{K_\alpha r_f}{U})p + K_{p|p|}p|p| \\ \qquad\qquad + K_{\phi UU}U^2\phi - K_\phi \sin(\phi) - 2K_\alpha\alpha \end{cases} \tag{1.6}$$

For compactness, six coefficients can be introduced:

$$\begin{cases} \dot{\phi} = p \\ A\dot{p} = Bp + Cp|p| + D\phi + E\sin(\phi) + F\alpha \end{cases} \tag{1.7}$$

where:

$$A = I_X - K_{\dot{p}} \tag{1.8}$$

$$B = K_p + K_{Up}U - 2\frac{K_\alpha r_f}{U} \tag{1.9}$$

$$C = K_{p|p|} \tag{1.10}$$

$$D = K_{\phi UU}U^2 \tag{1.11}$$

$$E = -K_\phi \tag{1.12}$$

$$F = -2K_\alpha \tag{1.13}$$

Normalizing the parameters to A yields the nondimensional form that will be used throughout this work. Lowercase letters represent the normalized parameters[1]. The state space variables used for the representation are $x_1 = \phi, x_2 = p$. The control input u is the mechanical fin angle α. The final form of the system is provided in the following equations.

$$\begin{cases} \dot{x}_1 = x_2 \\ \dot{x}_2 = bx_2 + cx_2|x_2| + dx_1 + e\sin(x_1) + \varphi u \end{cases} \tag{1.14}$$

$$f(\mathbf{x}) = \begin{bmatrix} x_2 \\ bx_2 + cx_2|x_2| + dx_1 + e\sin(x_1) \end{bmatrix} \tag{1.15}$$

$$g(x) = \begin{bmatrix} 0 \\ \varphi \end{bmatrix} \tag{1.16}$$

[1]Here, and throughout this work, the parameter φ will represent F/A to make a distinction with the function $f(\mathbf{x})$

Parameters list		
Parameter	Value	Meaning
U	15	Nominal forward speed [knots]
Ix	3.4263E6	Roll inertia $[Kg \cdot m^2]$
rf	4.22	Arm from fin forces to center of gravity $[m]$
A_f	1.7	Fin area $[m^2]$
C_l	0.046	Linear lift coefficient $[N/\text{deg}]$
ρ	1025	Water density $[kg/m^2]$
g	9.81	Gravity acceleration $[m/s^2]$
V	355.88	Volume displacement $[m^3]$
GMt	1	Transverse Metacentric Height $[m]$
$K_{\dot{p}}$	-0.674E6	Added inertia coefficient
K_p	-0.5E6	Linear damping coefficient
$K_{p\|p\|}$	-0.416E6	Nonlinear damping coefficient
K_{Up}	-15.5	Added Linear damping coefficient
$K_{\phi UU}$	-1180	Added restoring moment coefficient
Computed parameters		
$K_\alpha = 0.5\rho U^2 A_f C_l$		
$K_\phi = \rho g V \text{GMt}$		
State space coefficients		
Coefficient	Value	
b	-0.1232	
c	-0.1015	
d	-0.0648	
e	-0.8727	
φ	-0.0044	

Table 1.1: Parameters and coefficients

To aid in interpreting the results, the system's output is the roll angle expressed in degrees:

$$y = \frac{180}{\pi} x_1 \;\Rightarrow\; h(\mathbf{x}) = \frac{180}{\pi} x_1 \tag{1.17}$$

Chapter 2

Analysis

In this chapter, we will analyse the internal and structural stability of the dynamic model obtained in Chapter 1.

$$\begin{cases} \dot{x}_1 = x_2 \\ \dot{x}_2 = bx_2 + cx_2|x_2| + dx_1 + e\sin(x_1) + \varphi u \end{cases} \tag{2.1}$$

First, we will examine the equilibrium points and their stability properties with the nominal parameters. Then, we will use numerical methods to look for codimension 1 bifurcations under parameters variations. This study will initially be conducted without regard to the physical meaning of the variables and parameters. Finally, the mathematical results obtained from the model in Equation 2.1 will be interpreted in the context of the real system, allowing us to draw conclusions about its stability properties.

2.1 Equilibrium points

To find the equilibrium points, the following system of nonlinear equations must be solved:

$$\begin{cases} \dot{x}_1 = 0 \\ \dot{x}_2 = 0 \end{cases} \quad \Longrightarrow \quad \begin{cases} x_2 = 0 \\ dx_1 + e\sin(x_1) = 0 \end{cases} \tag{2.2}$$

The first equilibrium point is the trivial solution $(0, 0)$. The existence of other solutions depends on the parameters d and e. To determine whether other solutions to the second equation exist for the given parameters, the intersections between the curves $y = dx$ and $y = -e\sin(x)$ can be found numerically. Clearly, these intersection points will depend on the values of d and e.

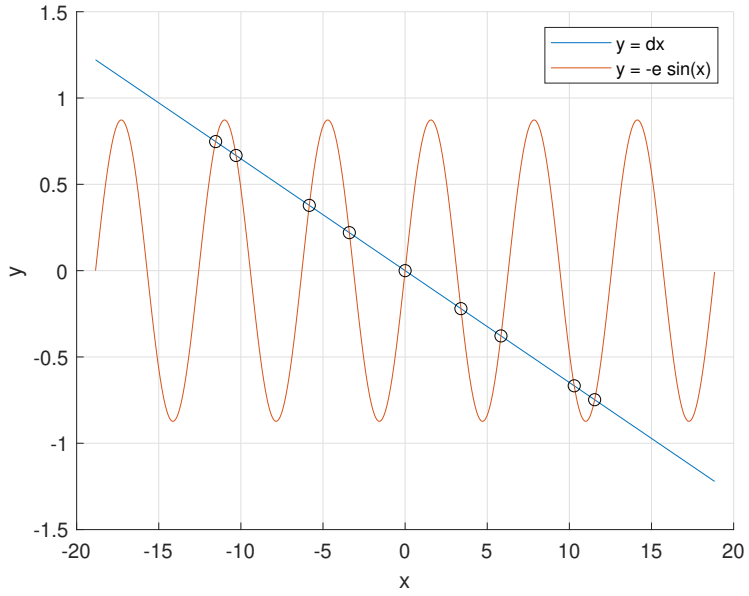

Figure 2.1: Solutions to $f_2(x_1, 0) = 0$ with the nominal parameters in Table 1.1

As shown in Figure 2.1, the two curves intersect in 9 different points. Therefore, the system with the nominal parameters has 9 equilibrium points. To study the stability of each equilibrium point, it is useful to compute the Jacobian.

$$J_f(\mathbf{x}) = \begin{bmatrix} 0 & 1 \\ d + e\cos(x_1) & b + 2c|x_2| \end{bmatrix} \tag{2.3}$$

$$J_f(0,0) = \begin{bmatrix} 0 & 1 \\ d + e & b \end{bmatrix} \tag{2.4}$$

If the Jacobian evaluated at the equilibrium point has no eigenvalues with zero real parts, the equilibrium point is said to be hyperbolic. Hartman-Grossman theorem states that the behaviour of a dynamical system near a hyperbolic equilibrium point is qualitatively the same as the behaviour of its linearization in this equilibrium point. For example, since $J_f(0,0)$ in Equation 2.4 has a pair of complex eigenvalues with negative real parts, the origin is an hyperbolic equilibrium point and we can conclude that it is LAS.

Table 2.1 lists all the equilibrium points, along with the eigenvalues of the linearized system and the type of equilibria.

Phase plane analysis is also performed to further study the behavior of the system. In Figure 2.2, the red dots represent the equilibrium points. Some trajectories are drawn in blue, and the nullclines are represented by the dashed orange and pink lines. The

Equilibrium points		
Point (x_1, x_2)	Eigenvalues	Type
$(-11.5376, 0)$	$-0.062 \pm 0.71i$	Spiral sink.
$(-10.2949, 0)$	$-0.77;\ 0.65$	Saddle point.
$(-5.8351, 0)$	$-0.062 \pm 0.92i$	Spiral sink.
$(-3.3965, 0)$	$-0.95;\ 0.82$	Saddle point.
$(0, 0)$	$-0.062 \pm 0.97i$	Spiral sink.
$(3.3965, 0)$	$-0.95;\ 0.82i$	Saddle point.
$(5.8351, 0)$	$-0.062 \pm 0.92i$	Spiral sink.
$(10.2949, 0)$	$-0.77;\ 0.65$	Saddle point.
$(11.5376, 0)$	$-0.062 \pm 0.71i$	Spiral sink.

Table 2.1: Equilibrium points of the system

equations of the nullcline curves are:

$$x_2 = 0 \tag{2.5}$$

$$bx_2 + cx_2|x_2| + dx_1 + e\sin(x_1) = 0 \tag{2.6}$$

2.2 Ruling out closed orbits

The existence of limit cycles can be easily excluded using the Dulac criterion: if the divergence of the vector field is neither zero nor changes sign, then there cannot be limit cycles.

$$\operatorname{div}(f) = \frac{\partial f_1}{\partial x_1} + \frac{\partial f_2}{\partial x_2} = b + 2c|x_2| < 0 \quad \forall \mathbf{x} \in \mathbb{R}^2 \tag{2.7}$$

2.3 Structural stability

Structural stability refers to the robustness of the system to perturbations of its structure. In this section, we will look for codimension 1 bifurcations, meaning we will vary one parameter at a time for the bifurcation to occur

Parameter b

The b parameter does not appear in Equation 2.2, meaning that a change in this parameter will not change the number of equilibrium points. However, for a planar system the equilibria can be characterized just by looking at the trace and determinant of the Jacobian.

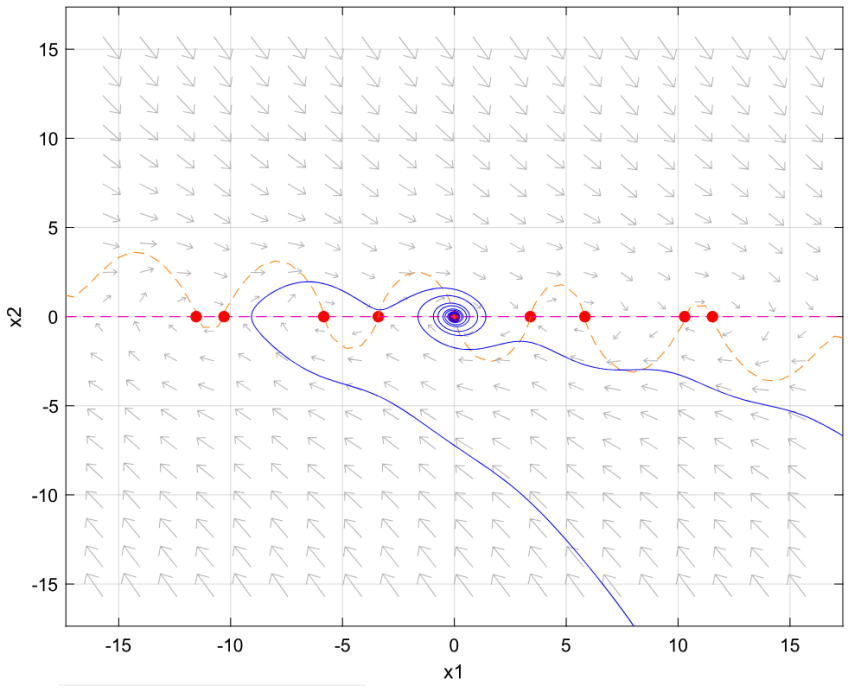

Figure 2.2: Phase plane analysis

Focusing on the equilibrium point $(0, 0)$, its trace and determinant are as follows:

$$\begin{cases} \tau = b \\ \Delta = -d - e \end{cases} \tag{2.8}$$

The eigenvalues of the Jacobian are $\lambda_{1,2} = \frac{\tau \pm \sqrt{\tau^2 - 4\Delta}}{2}$. With nominal values of d and e being negative, when b transitions from negative to positive, it shifts from a stable spiral/node to an unstable spiral/node. Numerical analysis using Matcont [5] reveals that when b reaches zero, the origin undergoes a Hopf bifurcation, resulting in a stable limit cycle around it. All the previously stable equilibria become unstable, and trajectories converge to this limit cycle. Figure 2.3 illustrates the limit cycle, and Figure 2.4 shows sample trajectories converging on the limit cycle.

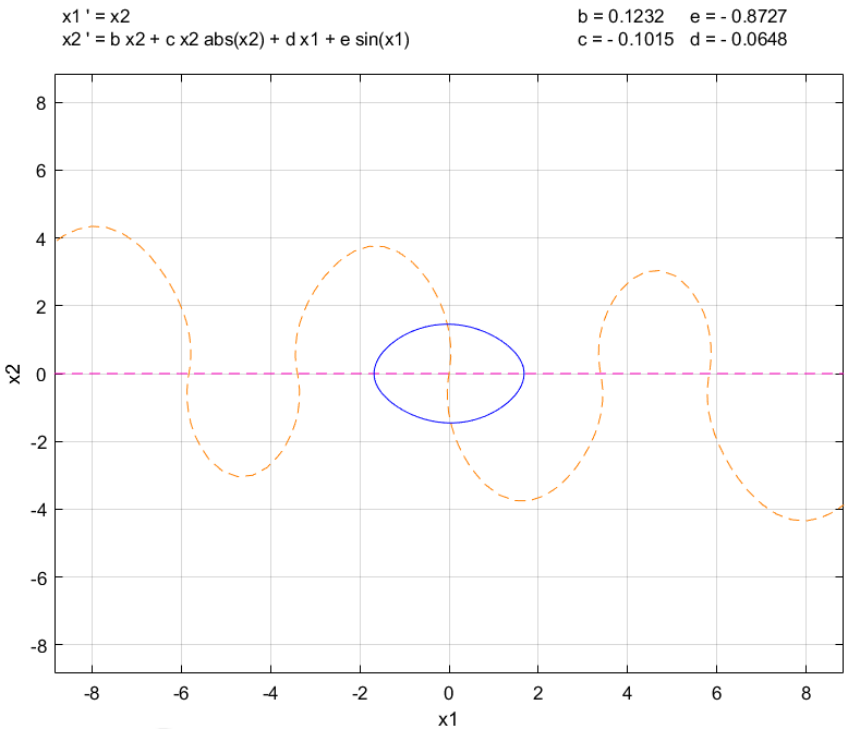

Figure 2.3: Closed orbit generated when $b > 0$

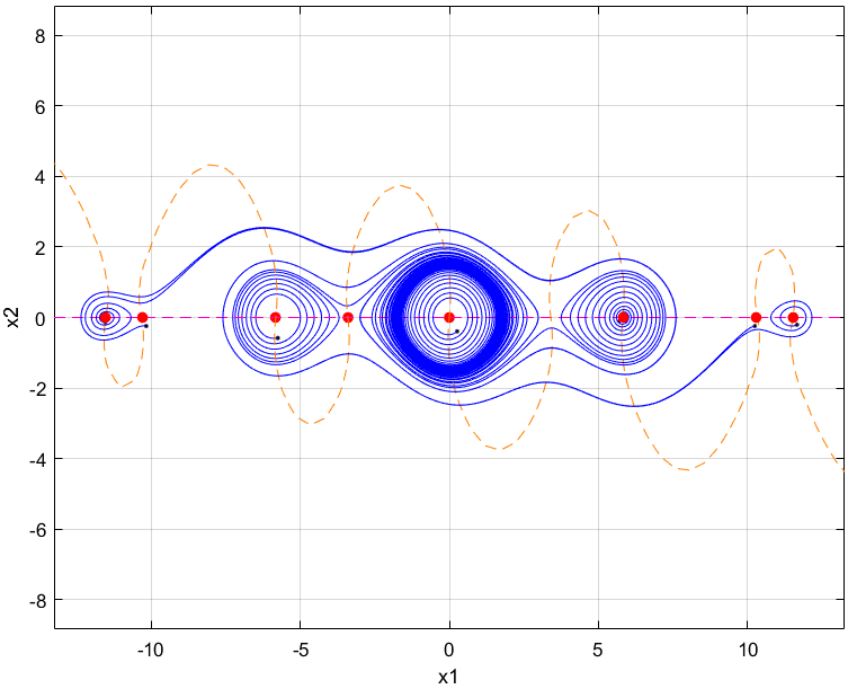

Figure 2.4: Example of forward in time trajectories converging on the limit cycle after the Hopf bifurcation: $b > 0$

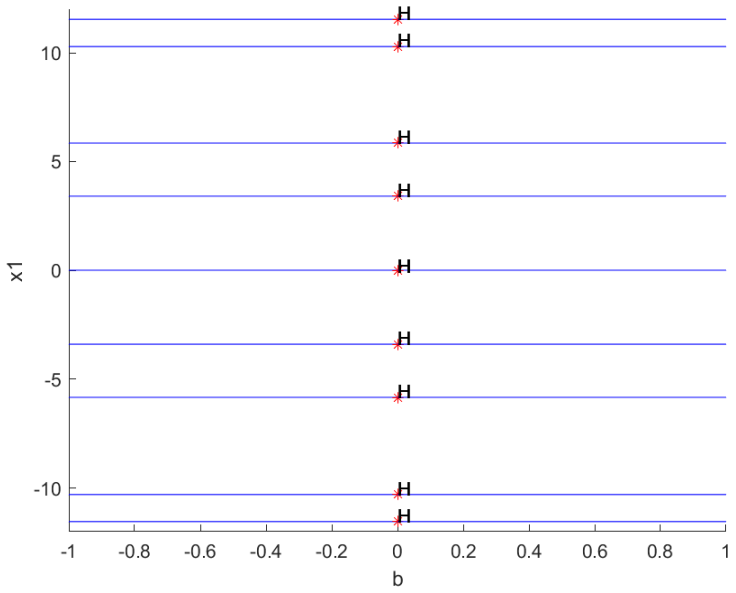

Figure 2.5: Matcont bifurcation diagram for the parameter b

Parameter c

The parameter c does not appear neither in the equilibrium points equation not in the Jacobian, meaning that the number and the position of the equilibria will not change. The local stability properties of the equilibria will also not change. Hence, a variation of the parameter c does not lead to any local bifurcation. However, the vector field f will still change, and further numerical analysis should be carried out to understand if there is any global bifurcation taking place. Tools like Matcont, that rely on the Jacobian of the system, and therefore on local arguments, cannot be used. To find out whether a limit cycle is generated, we can use a Poincaré Map. Considering the following Poincaré plane:

$$\Sigma = \{\mathbf{x} \in \mathbb{R}^2 : x_2 = 0\} \tag{2.9}$$

we define the Poincaré Map $P : \Sigma \to \Sigma$ with crossing direction $\dot{x}_2 > 0$. The numerical algorithm is described in Algorithm 1.

Algorithm 1 Compute the Poincaré diagram

```
Input: Set of coefficients C, set of equilibrium points E
for each c ∈ C do
    for each equilibrium point e ∈ E do
        Initialize a grid of initial conditions near e
        for each initial condition x_0 in the grid do
            Compute forward system flow starting from x_0
            Compute backward system flow starting from x_0
            Find intersections with the Poincaré map
        end for
        Find the steady state values of intersections
    end for
end for
Output: Equilibria of the Poincaré Map
```

The results of the numerical analysis are shown in Figure 2.7. As soon as $c > 0$, a large unstable limit cycle is generated, and its dimension reduces as c increases. When crossing the equilibria, two unstable limit cycles are formed: one before and one after the equilibria. After the crossing, these two cycles merge into one again. After crossing all the equilibria, thus enclosing only the origin, the limit cycle keeps shrinking and other unstable limit cycles are generated around the other equilibria.

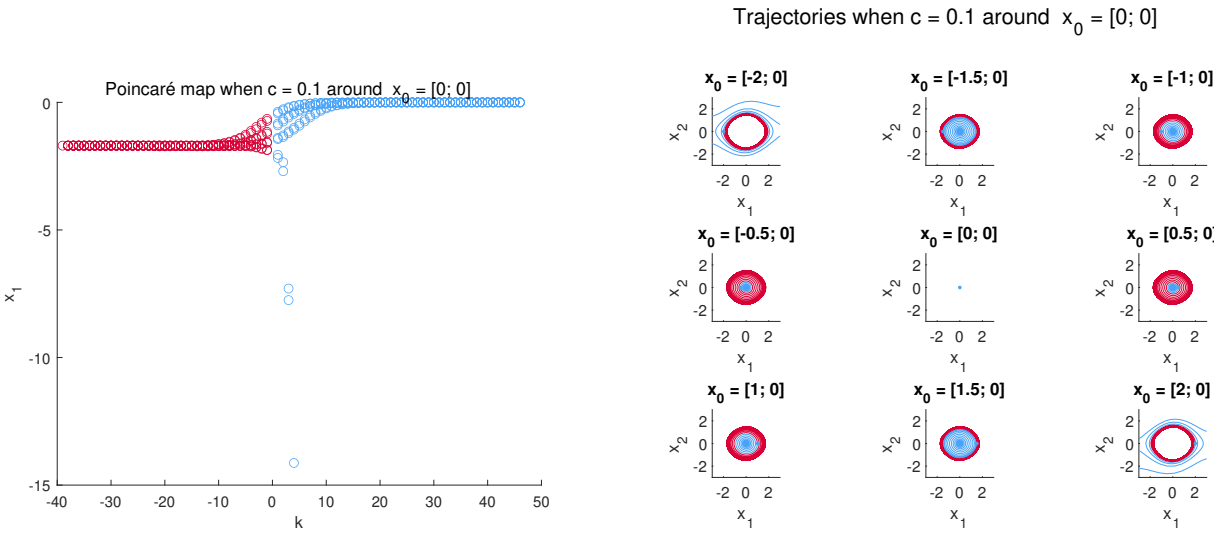

Figure 2.6: Forward (blue) and backward (red) trajectories of the Poincaré Map and the system. The analysis of the map evolution near (0, 0) highlights an equilibrium in (0, 0) and in (−1.7, 0). While the first is related to a stable spiral of the system, the latter is an unstable limit cycle.

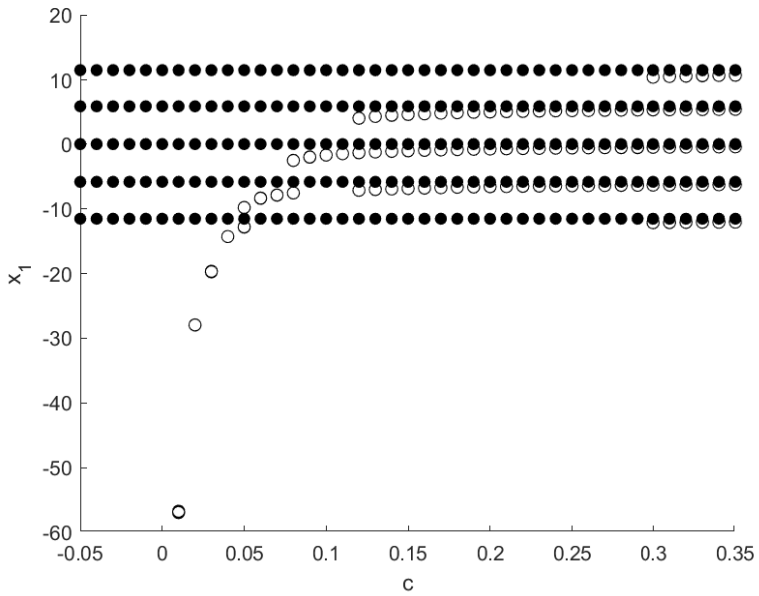

Figure 2.7: Stable (filled circles) and unstable (empty circles) equilibrium points of the Poincaré Map.

Parameter d

From Figure 2.1, it is evident that reducing the value of d increases the steepness of the line. While the point (0, 0) remains unchanged, the saddles collide with the stable equilibria and disappear, leading to Saddle Node bifurcations. However, when d becomes larger, and eventually exceeds $-e$, the two saddles closest to the origin will collide with the stable equilibrium (0, 0). Figure 2.8 graphically shows this intuition. The trace

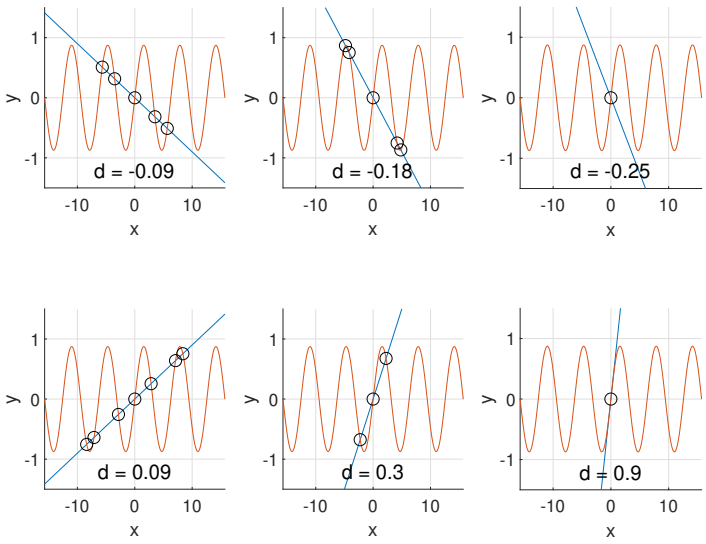

Figure 2.8: Intersections for different values of d

determinant analysis, according to Equation 2.8, indicates that the origin transforms into a saddle. This kind of behavior highlights a subcritical pitchfork bifurcation, as confirmed by the numerical analysis represented in Figure 2.9. The complete bifurcation diagram is obtained using Matcont, and is represented in Figure 2.10.

Parameter e

Similarly to the parameter d, a variation of the parameter e gives rise to Saddle Node bifurcations and a pitchfork bifurcation, as can be immediately understood from Figure 2.1. However, a numerical analysis of the Jacobian and its eigenvalues shows that in this case, when $e = -d$, we get a supercritical pitchfork bifurcation.

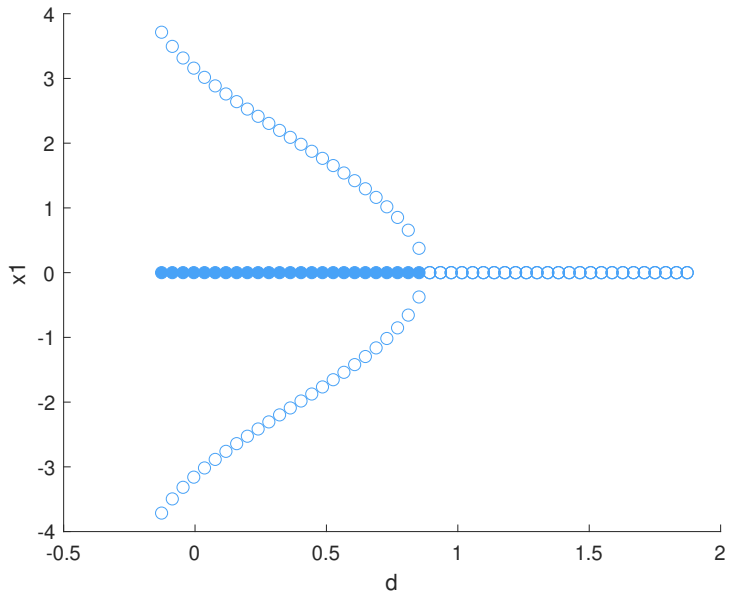

Figure 2.9: Equilibria around the origin and their stability when varying d: the empty circle represents an unstable equilibrium whereas the full circle represents a stable one

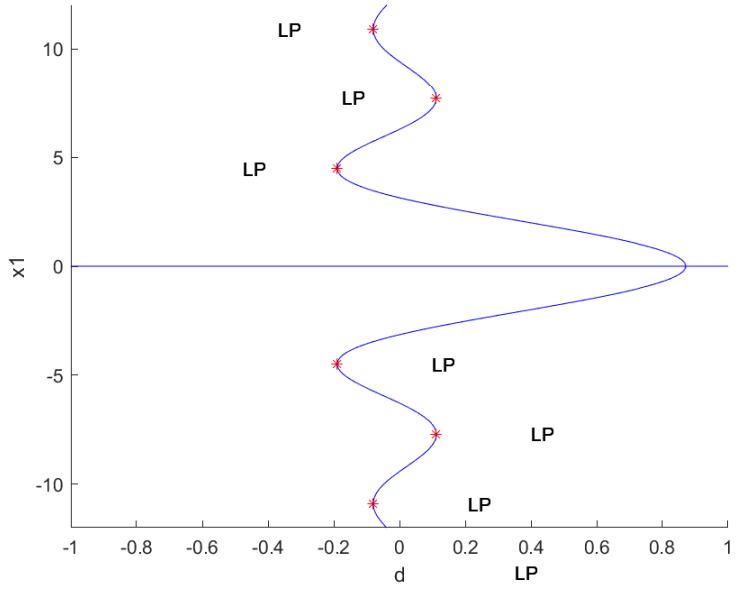

Figure 2.10: Matcont bifurcation diagram for the parameter d

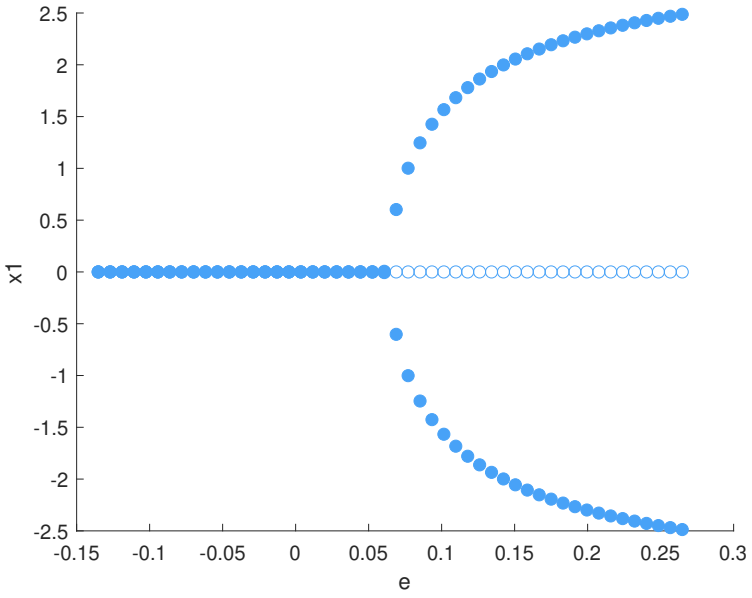

Figure 2.11: Equilibria around the origin and their stability when varying e

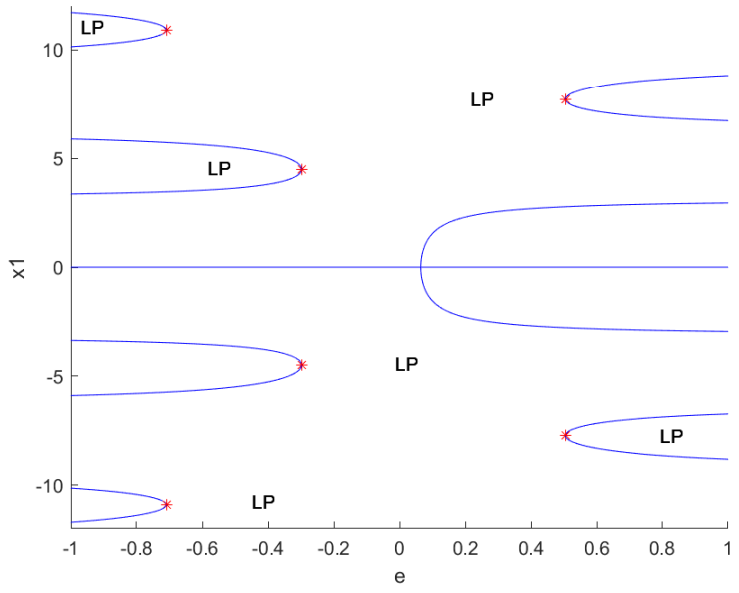

Figure 2.12: Matcont bifurcation diagram for the parameter e

2.4 Interpretation of results on the real system

The variable x_1 represents the roll angle of the vessel: the equilibrium point $(0, 0)$ describes the vessel in the upright attitude, without roll motion. The next equilibrium points are $(\pm 3.3965, 0)$ and correspond to the vessel almost in the vertical upside-down attitude. Although this is indeed an equilibrium point of the dynamical system in Equation 1.14, this is not true for the real physical system of a vessel in the sea. Beyond normal operating roll angles, the dynamics of the vessel will not be described by the model in Equation 1.6 due to higher order dynamics that are being neglected.

The equilibrium in $(0, 0)$ is the only one of interest. The linearized system analysis shows us that it is asymptotically stable, however, it is necessary to study the region of asymptotic stability to understand how the system behaves when the trajectories start far away from the equilibrium point. To estimate it, a numerical approach was used: a 30×30 grid of initial conditions is generated within the square with vertices $(-3.5, -3.5)$ and $(3.5, 3.5)$. Then, all the 900 simulations are run to distinguish the initial conditions that lead to the equilibrium point under investigation from those that do not. Figure 2.13

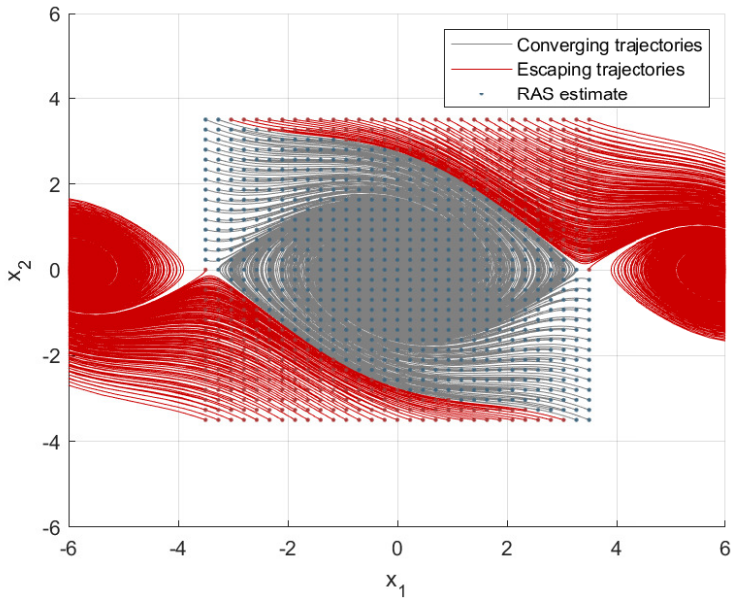

Figure 2.13: Numerical simulation for RAS estimation of the equilibrium (0, 0)

shows that RAS is large enough to include normal operating values of roll angles and roll velocities. Therefore, the open loop system doesn't show instability problems.

Regarding structural stability, in the previous paragraph we saw that the stability properties of the origin change only when the parameters become greater than zero. However, the physical meaning of these parameters doesn't allow them to be positive. Thus, we conclude that the system is structurally stable under any physically meaningful parameter variations.

Chapter 3

Synthesis

In this chapter, we will first outline the control objectives. Next, we will apply one linear and two nonlinear control techniques to the nominal system. All the controllers will be tested under sinusoidal disturbances in input. Testing the controllers under parameter uncertainty will be covered in the next chapter, where we will highlight the differences and strengths of each controller.

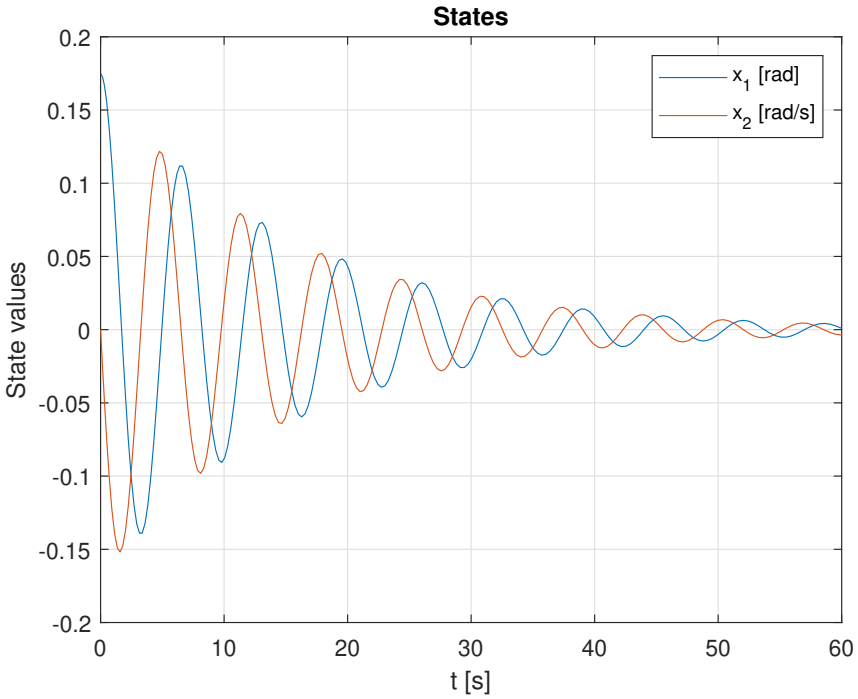

Figure 3.1: Free evolution of the states starting from $x_0 = [0.1745, 0]^\top$

3.1 Control objectives

The origin of the system is an asymptotically stable equilibrium. Figure 3.1 shows the free evolution of the system with $x_0 = [0.1745,\ 0]^\top$, corresponding to an initial roll angle of 10 degrees.

The control objective is to bring the system output $y = \frac{180}{\pi} x_1$ to 0 with a maximum 10% settling time of $10s$ and zero steady-state error, while minimizing transient oscillations. The closed loop system should damp the oscillations due to the sea waves. The wave disturbance is modeled as an input disturbance d as it follows.

$$d = \frac{F_w}{\varphi} \sin(\omega_w t) \tag{3.1}$$

so that:

$$\begin{cases} \dot{x}_1 = x_2 \\ \dot{x}_2 = b x_2 + c x_2 |x_2| + d x_1 + e \sin(x_1) + \varphi u + F_w \sin(\omega_w t) \end{cases} \tag{3.2}$$

The frequency ω_w of the disturbance will range from 0.3 rad/s to 1.3 rad/s, while the amplitude F_w will be up to 0.1 rad/s^2. The initial condition used for the simulations will be $x_0 = [0.1745,\ 0]^\top$.

Furthermore, since the control action is the physical angle between the fin and the flow of water, it must be small enough to stay away from stall conditions. The maximum angle depends on various factors, such as the shape of the fin. In this project, the maximum admissible value will be considered 20 deg. A saturation to such value will be added to ensure that this value will be never exceeded.

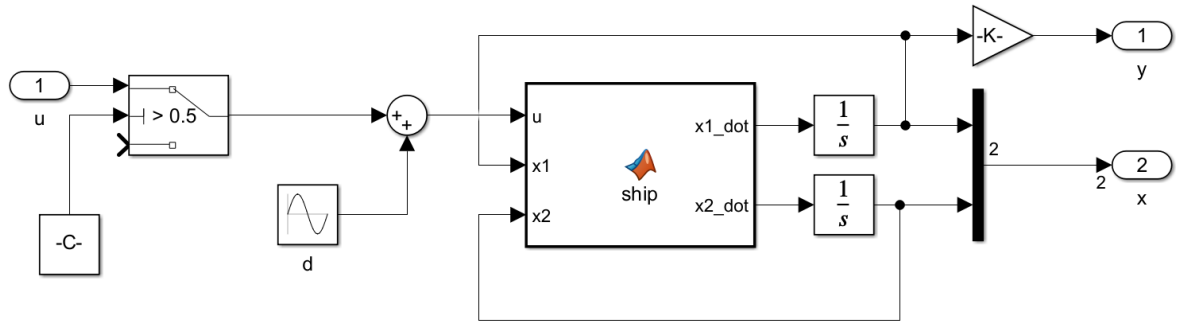

Figure 3.2: Model simulation scheme[1]

[1]The switch block in input is used by automated plot scripts to switch between the controlled and the uncontrolled system.

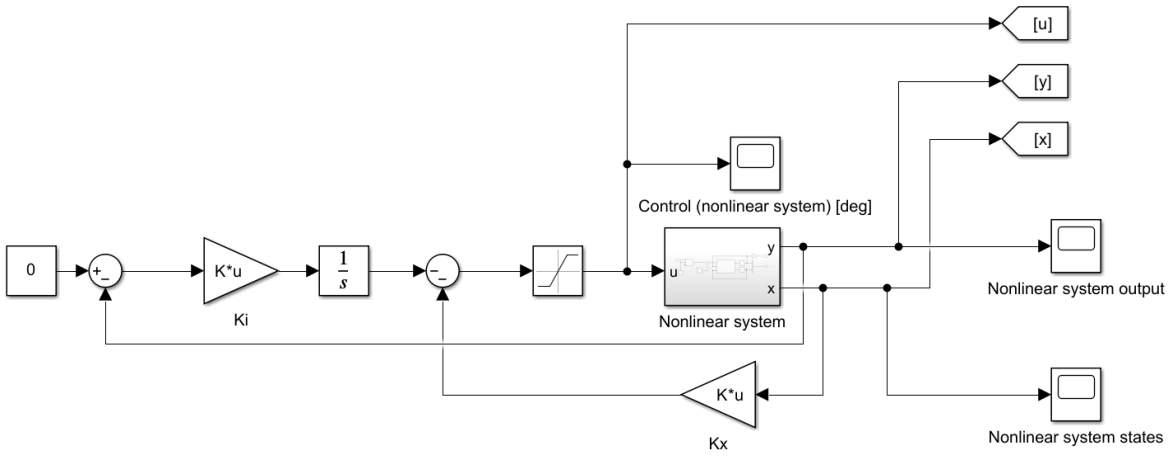

Figure 3.3: LQR control scheme

Table 3.1 shows the settling time and the oscillations amplitude of the open loop system.

Uncontrolled		
	$\omega = 0.3$	$\omega = 1.3$
Amplitude [deg]	6.65	7.34
Ts (10 deg - 1 deg)	35.7s	

Table 3.1: Uncontrolled system behavior

3.2 Linear control strategy (LQR)

Linear control strategies are based on the linearization of the system around the origin:

$$\dot{\mathbf{x}} = A_{\text{lin}}\mathbf{x} + B_{\text{lin}}u \tag{3.3}$$

$$y = C_{\text{lin}}\mathbf{x} \tag{3.4}$$

where:

$$A_{\text{lin}} = \begin{bmatrix} 0 & 1 \\ d+e & b \end{bmatrix}, \quad B_{\text{lin}} = \begin{bmatrix} 0 \\ \phi \end{bmatrix}, \tag{3.5}$$

$$C_{\text{lin}} = \begin{bmatrix} \frac{180}{\pi} & 0 \end{bmatrix}, \quad D_{\text{lin}} = 0$$

LQR control involves finding the state feedback gains K that minimize the objective function J:

$$J = \int_0^{+\infty} \mathbf{x}^T Q\mathbf{x} + u^T Ru \, \mathrm{d}t \tag{3.6}$$

The matrices Q and R penalize respectively high values of the state and control inputs. The values are chosen by trial and error until the output with the desired characteristics is obtained. Since state feedback alone does not ensure zero steady-state error and robustness to model uncertainties, an augmented system with an integrator is considered, with matrices as follows:

$$\begin{gathered} A_{\text{int}} = \begin{bmatrix} A_{\text{lin}} & \mathbf{0}_{2\times 1} \\ -C_{\text{lin}} & 0 \end{bmatrix}, \quad B_{\text{int}} = \begin{bmatrix} B_{\text{lin}} \\ -D_{\text{lin}} \end{bmatrix}, \\ C_{\text{int}} = \begin{bmatrix} C_{\text{lin}} & 0 \end{bmatrix}, \quad D_{\text{int}} = D_{\text{lin}} \end{gathered} \tag{3.7}$$

The state vector of this system now has three components: $\mathbf{x} = [x_1, x_2, x_I]^\top$, where x_I is the integral of the error over time.

Controller parameters	
Q	diag([100000, 300000, 4])
R	0.3
K	(−236.0635, −582.1940, 2.2361)

Table 3.2: LQR Parameters

With the parameters in Table 3.2, the controller achieves a settling time of 6.89s with an acceptable transient, achieving the same results both on the linearized and on the nonlinear system. Table 3.3 summarizes the performance of the controller on the nonlinear system.

LQR		
	$\omega = 0,3$	$\omega = 1,3$
Amplitude [deg]	1.34	1.29
Reduction	-79.85%	-82.43%
Ts (10 deg - 1 deg)	6.89s	

Table 3.3: LQR controller results

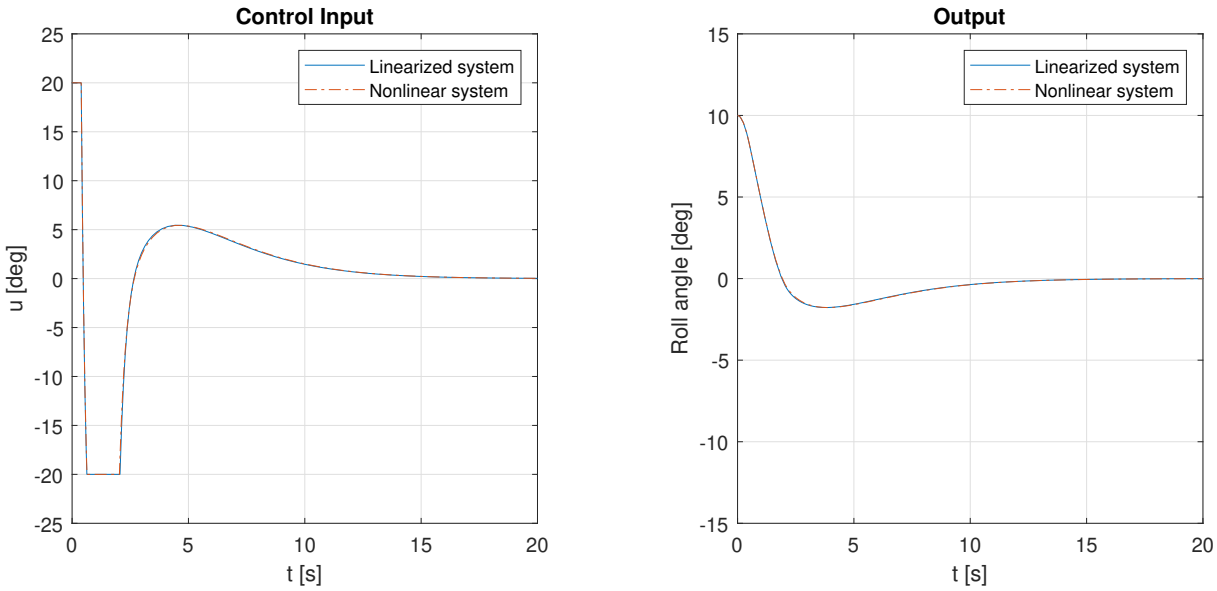

Figure 3.4: System output and control input with the LQR controller, no waves

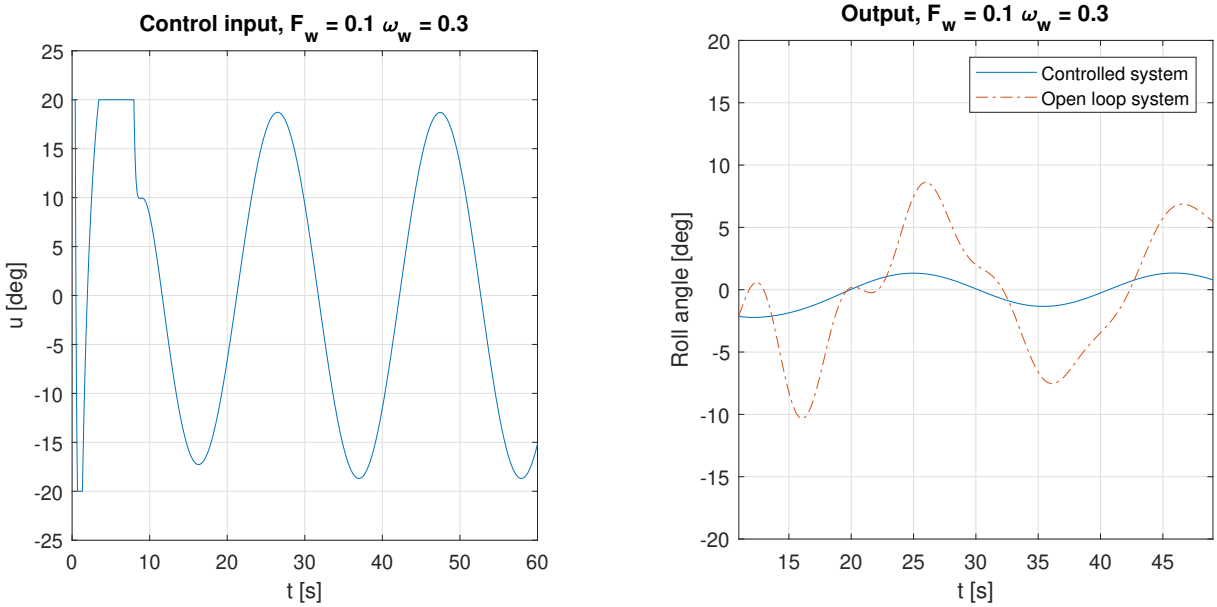

Figure 3.5: System output and control input with the LQR controller, $\omega_w = 0.3$

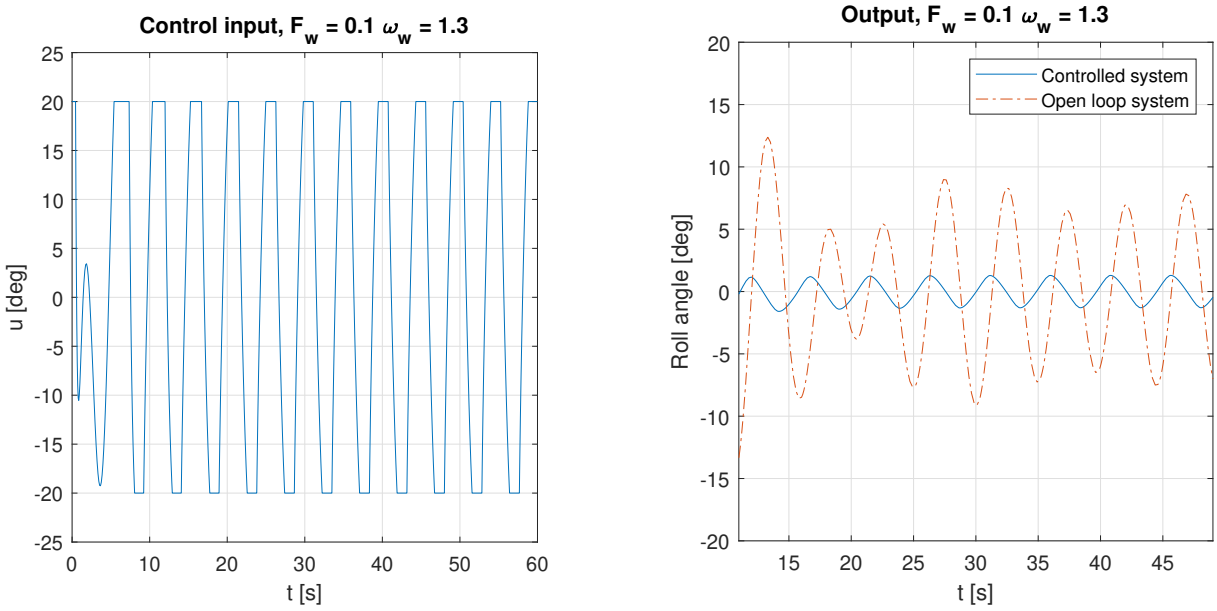

Figure 3.6: System output and control input with the LQR controller, $\omega_w = 1.3$

3.3 Feedback Linearization with LQR

For the system in Equation 1.14, IO feedback linearization implementation is straightforward. The output $y = h(\mathbf{x})$ can be differentiated until the input u appears:

$$\begin{aligned} \dot{y} &= \tfrac{180}{\pi}\dot{x}_1 = \tfrac{180}{\pi}x_2 \\ \ddot{y} &= \tfrac{180}{\pi}\left(bx_2 + cx_2|x_2| + dx_1 + e\sin(x_1) + \varphi u\right) \end{aligned} \tag{3.8}$$

Since the output must be differentiated two times to find the input, the relative degree of the system is two. Therefore, the system doesn't have internal dynamics. The goal of IO FBL is to find a control input that globally linearizes the system, and and turns it into the form $\ddot{y} = v$, where v is an auxiliary control input.

From Equation 3.8 it is evident that to achieve such goal, the input u must be chosen as:

$$u = -\frac{1}{\varphi}\left(bx_2 + cx_2|x_2| + dx_1 + e\sin(x_1) - \frac{\pi}{180}v\right) \tag{3.9}$$

Formally, this can be expressed as

$$u = -\frac{1}{\mathcal{L}_g\left(\mathcal{L}_f(h)\right)}\left(\mathcal{L}_f^2(h) - v\right) \tag{3.10}$$

where v is an auxiliary control input, and:

$$\mathcal{L}_f(h) = \nabla h \cdot f = \tfrac{180}{\pi} x_2 \tag{3.11}$$

$$\mathcal{L}_f^2(h) = \tfrac{180}{\pi} \left(b x_2 + c x_2 |x_2| + d x_1 + e \sin(x_1)\right) \tag{3.12}$$

$$\mathcal{L}_g \left(\mathcal{L}_f(h)\right) = \nabla \mathcal{L}_f(h) \cdot g = \tfrac{180}{\pi} \varphi \tag{3.13}$$

$$\tag{3.14}$$

When the control law in Equation 3.10 is applied to the system in Equation 1.14, the closed loop system becomes:

$$\begin{cases} \dot{x}_1 = x_2 \\ \dot{x}_2 = v \end{cases} \tag{3.15}$$

Of course, the saturation will degrade the performance of the feedback linearization when the limits are reached.

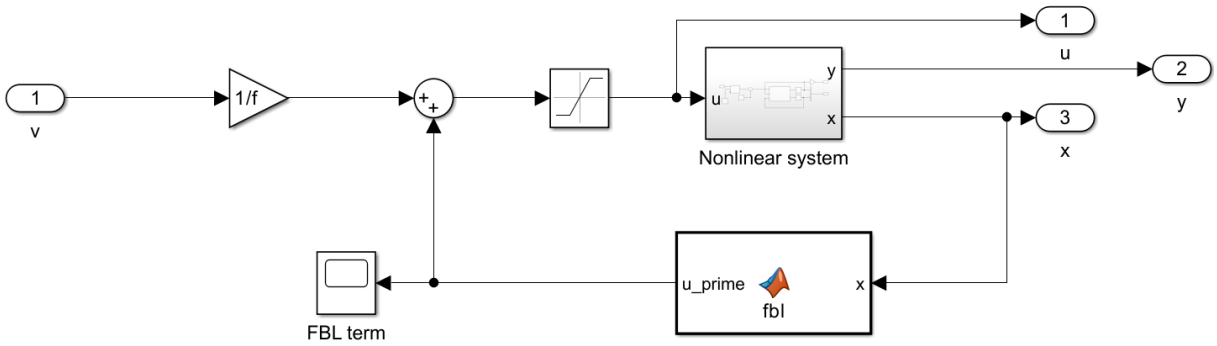

Figure 3.7: Feedback linearization control scheme

After globally linearizing the system, the auxiliary input v can be designed to control the linear system in Equation 3.15 to the desired values of x_1 and x_2. The choice of v is totally arbitrary. Again, an LQR controller with integral action has been used to find a trade off between performance and control action, and to add robustness to the system. Differently from the previous control technique, here the linear system that the outer LQR loop has to control is:

$$A_{\text{fbl}} = \begin{bmatrix} 0 & 1 \\ 0 & 0 \end{bmatrix}, \quad B_{\text{fbl}} = \begin{bmatrix} 0 \\ 1 \end{bmatrix}, \tag{3.16}$$

$$C_{\text{fbl}} = \begin{bmatrix} \frac{180}{\pi} & 0 \end{bmatrix}, \quad D_{\text{fbl}} = 0$$

Then, the design follows the same pattern as a standard LQR. The performance of FBL with LQR controller are shown in Table 3.5, and are very similar to the performance of the previous controller. The motivations will be discussed later in the controllers comparison.

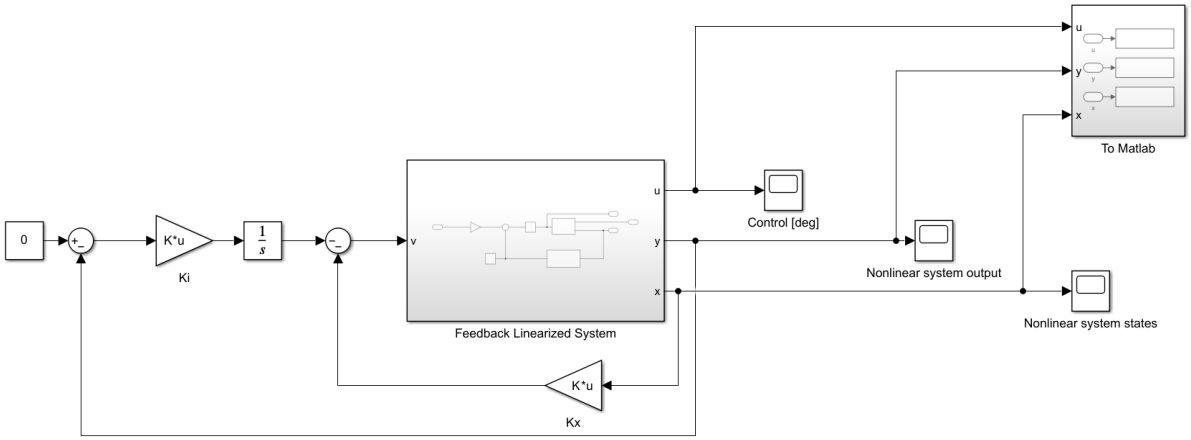

Figure 3.8: LQR loop on the feedback linearized system

Controller parameters	
Q	diag([1, 20, 0.001])
R	1
K	(4.5316, 5.3910, −0.0316)

Table 3.4: FBL + LQR Parameters

FBL + LQR		
	$\omega = 0,3$	$\omega = 1,3$
Amplitude [deg]	0.94	1.43
Reduction	-85.86%	-80.52%
Ts (10 deg - 1 deg)	6.24s	

Table 3.5: FBL + LQR controller results

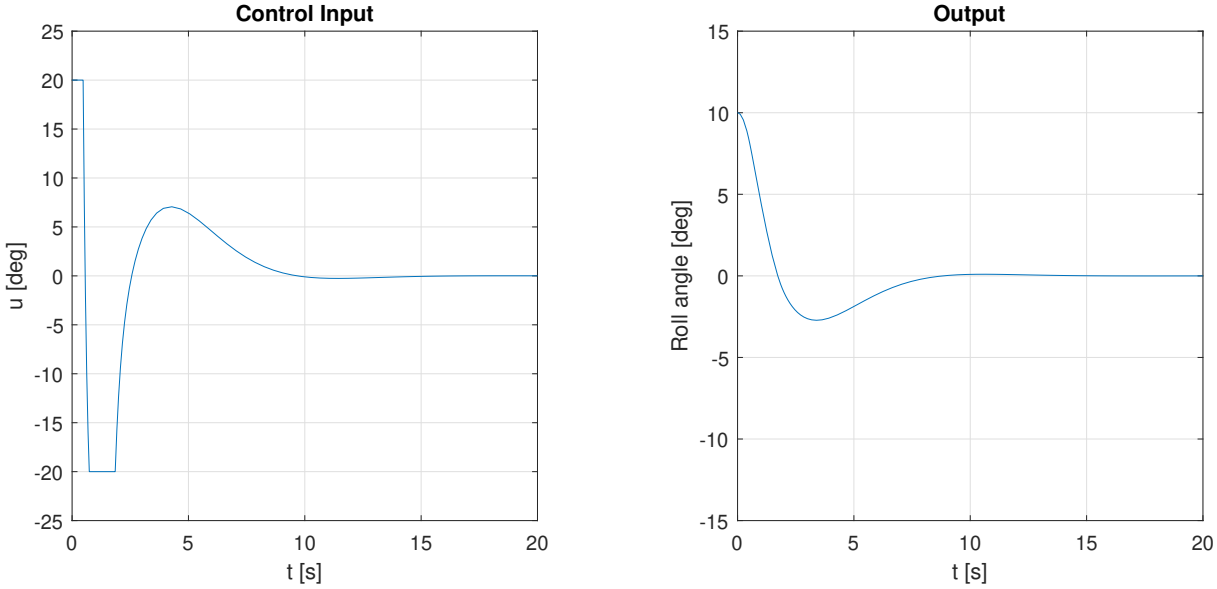

Figure 3.9: System output and control input with the FBL controller, no waves

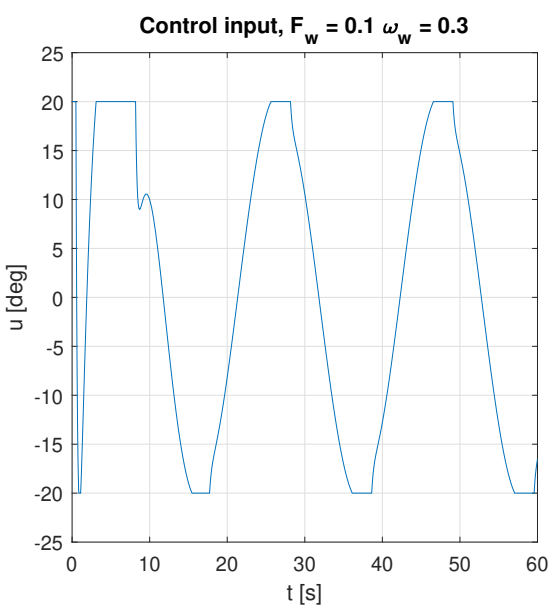

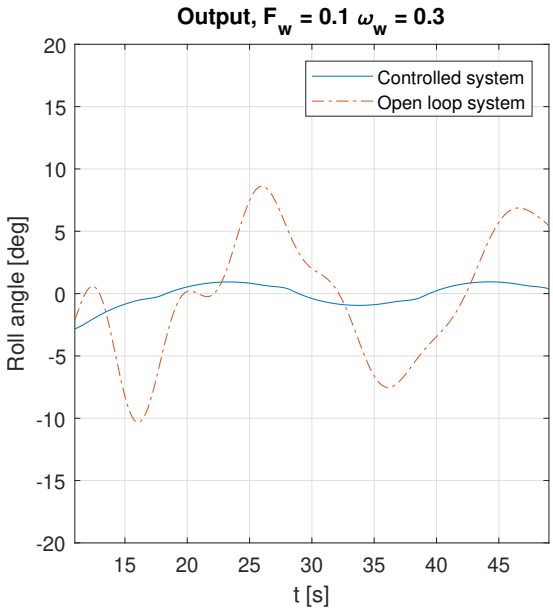

Figure 3.10: System output and control input with the FBL controller, $\omega_w = 0.3$

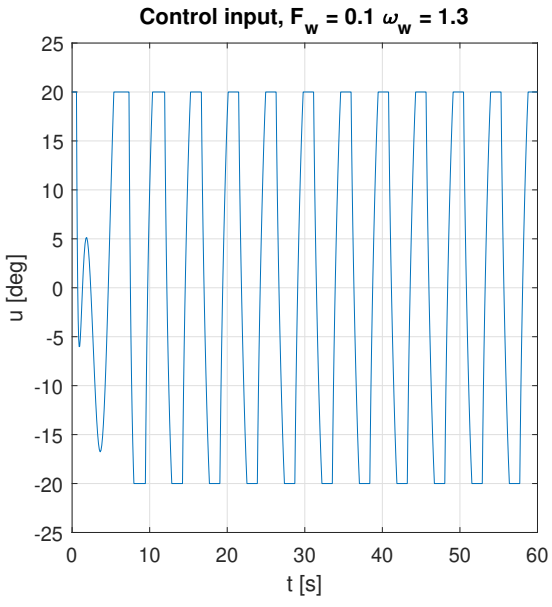

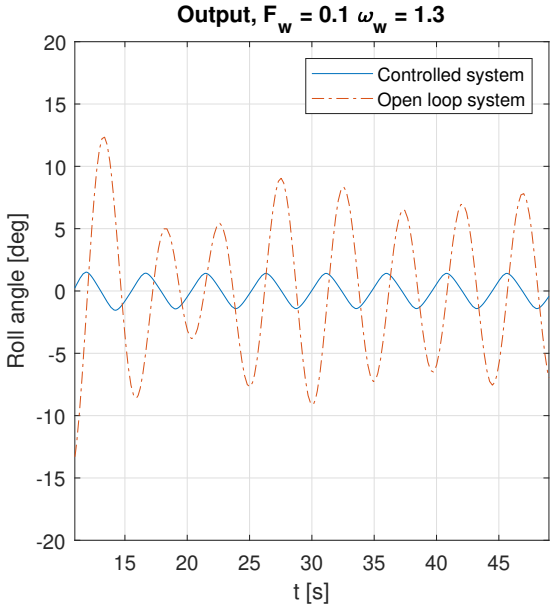

Figure 3.11: System output and control input with the FBL controller, $\omega_w = 1.3$

3.4 Sliding Mode Control

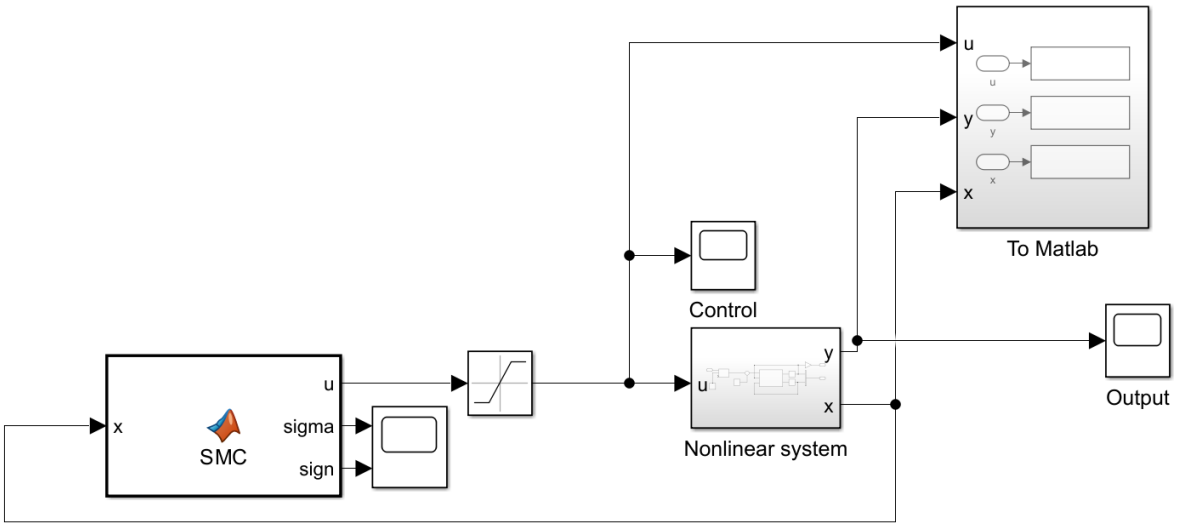

Figure 3.12: Sliding Mode Control scheme

Due to its robustness and ability to reject matched disturbances, Sliding Mode Control is a suitable candidate for the problem at hand. The sliding function $\sigma(\mathbf{x}) = p_1 x_1 + p_2 x_2$ defines a sliding surface $\Sigma = \mathbf{x} \in \mathbb{R}^2 :, \sigma(\mathbf{x}) = 0$ that satisfies the transversality condition:

$$\mathcal{L}_g(\sigma) = \nabla\sigma \cdot g = \begin{bmatrix} p_1 & p_2 \end{bmatrix} \begin{bmatrix} 0 \\ \varphi \end{bmatrix} = p_2\varphi \neq 0 \quad \forall \mathbf{x} \tag{3.17}$$

To make the sliding surface attractive, the switching control action in Equation 3.18 is be chosen.

$$u = -\frac{K}{\mathcal{L}_g(\sigma)} \operatorname{sign}(\sigma) - \frac{\mathcal{L}_f(\sigma)}{\mathcal{L}_g(\sigma)} \tag{3.18}$$

where

$$\mathcal{L}_f(\sigma) = \nabla\sigma \cdot f = p_1 x_2 + p_2(bx_2 + cx_2|x_2| + dx_1 + e\sin(x_1)) \tag{3.19}$$

The parameters p_1, and p_2 can be tuned based on the following considerations: on the sliding surface, when $\sigma(\mathbf{x}) = 0$, the equivalent control input is $u = -\frac{\mathcal{L}_f(\sigma)}{\mathcal{L}_g(\sigma)}$. Therefore, the closed-loop system equation can be found as:

$$\dot{\mathbf{x}} = f(\mathbf{x}) + g(\mathbf{x}) \left(-\frac{\mathcal{L}_f(\sigma)}{\mathcal{L}_g(\sigma)} \right) \tag{3.20}$$

The closed-loop system equations show that:

$$\begin{cases} \dot{x}_1 = x_2 \\ \dot{x}_2 = -\frac{p_1}{p_2} x_2 \end{cases} \tag{3.21}$$

Since, on the sliding surface $\sigma(\mathbf{x}) = 0 \Rightarrow x_2 = -\frac{p_1}{p_2} x_1 \Rightarrow \dot{x}_1 = -\frac{p_1}{p_2} x_1$, with a positive choice of the parameters p_1 and p_2, the origin is a globally asymptotically stable equilibrium point, and the settling time on the sliding surface is determined by the time constant $\tau = \frac{p_2}{p_1}$.Regarding the parameter K, a higher value will result in a faster convergence time on the sliding region and better rejection of matched disturbances, while increasing the amplitude of the switching control action.

While ideally, this solution would effectively control the system on the switching manifold, it would require an infinite commutation frequency while on Σ. To avoid such issue, known as Chattering, we consider a continuous approximation of the signum function: $\text{sat}_{\pm 1}(\sigma/\epsilon)$. This method reduces the commutation frequency while allowing a boundary layer around Σ, with a width that increases with ϵ. The performance is presented in Table 3.7.

Control parameters	
p_1	5
p_2	10
K	5
ϵ	$1 \cdot 10^{-4}$

Table 3.6: SMC parameters

SMC		
	$\omega = 0,3$	$\omega = 1,3$
Amplitude [deg]	0.91	0.6
Reduction	-86.32%	-91.83%
Ts (10 deg - 1 deg)	2.08s	

Table 3.7: SMC results

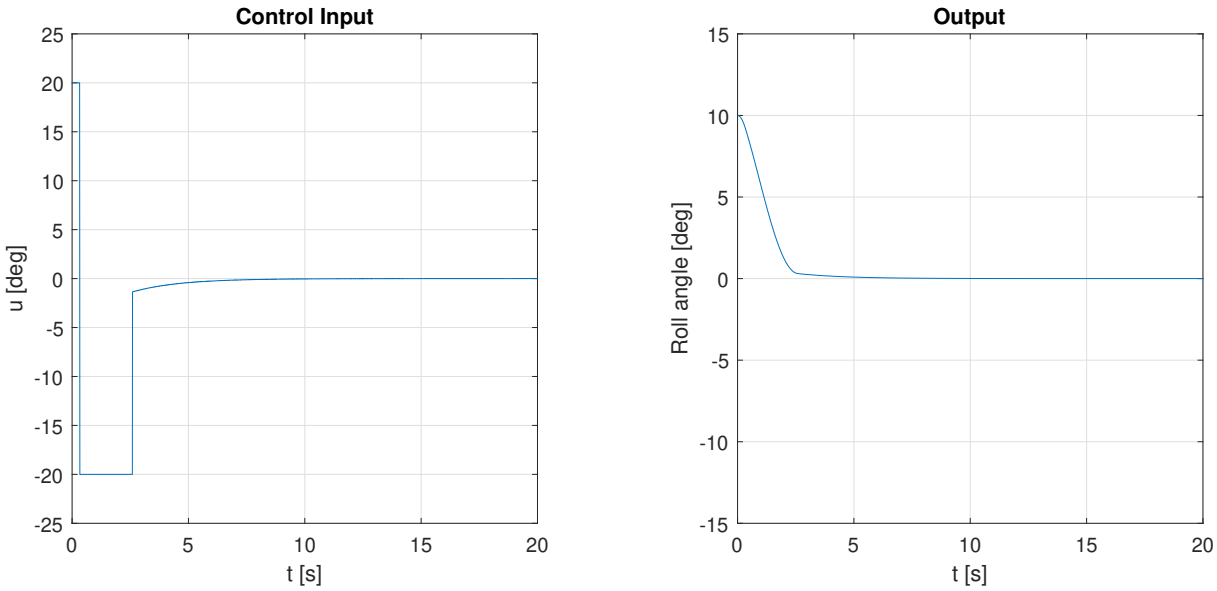

Figure 3.13: System output and control input with the SMC controller, no waves

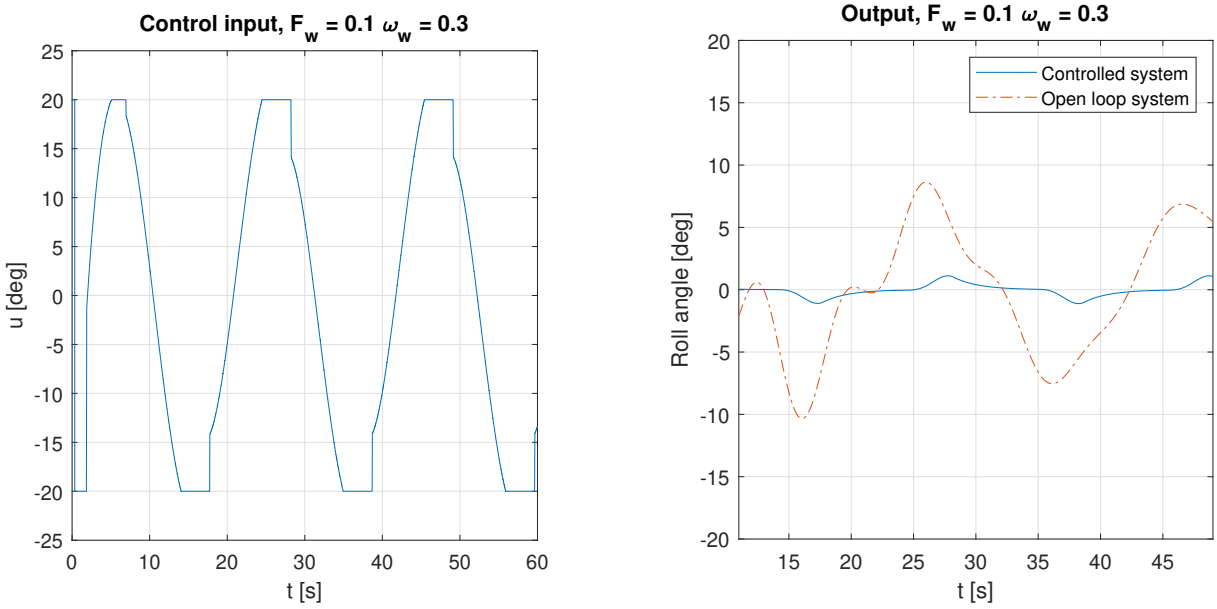

Figure 3.14: System output and control input with the SMC controller, $\omega_w = 0.3$

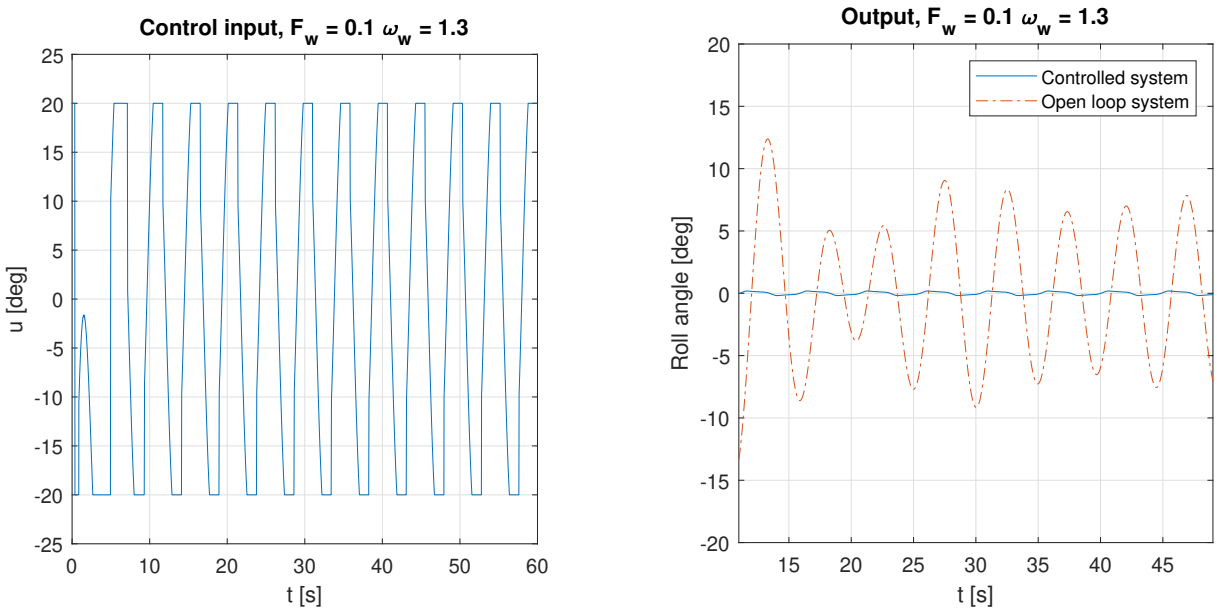

Figure 3.15: System output and control input with the SMC controller, $\omega_w = 1.3$

Chapter 4

Controller robustness and comparison

Before comparing the controllers, their performances must be assessed under parameter uncertainties, as it is difficult to precisely estimate all the parameters listed in Table 1.1. In this chapter, we will first test the controllers under various parametric errors and then compare the performance of the three controllers on both the nominal and uncertain systems.

4.1 Parameters uncertainty

By denoting the real parameters of the system as α_r, the controllers will be tuned on the parameters $\alpha = \alpha_r/(1+\varepsilon)$ and tested on the system with real parameters α_r. The error ε will vary between -0.5, -0.1, 0.1, and 0.5, and the controllers will be tested both with no disturbance, and with two sinusoidal disturbances of frequency 0.3 rad/s and 1.3 rad/s.

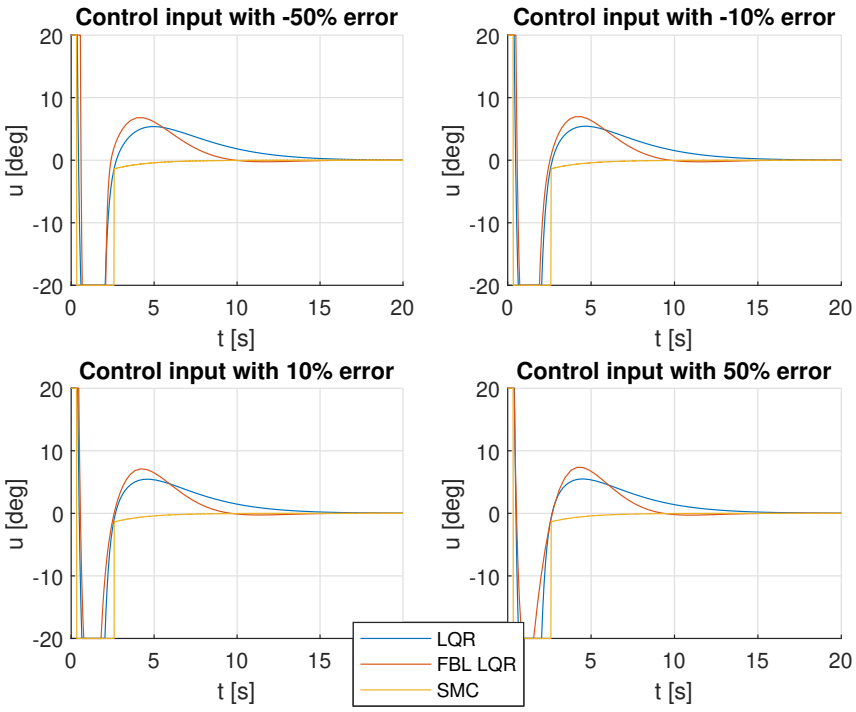

Figure 4.1: Control input with uncertainty, no waves

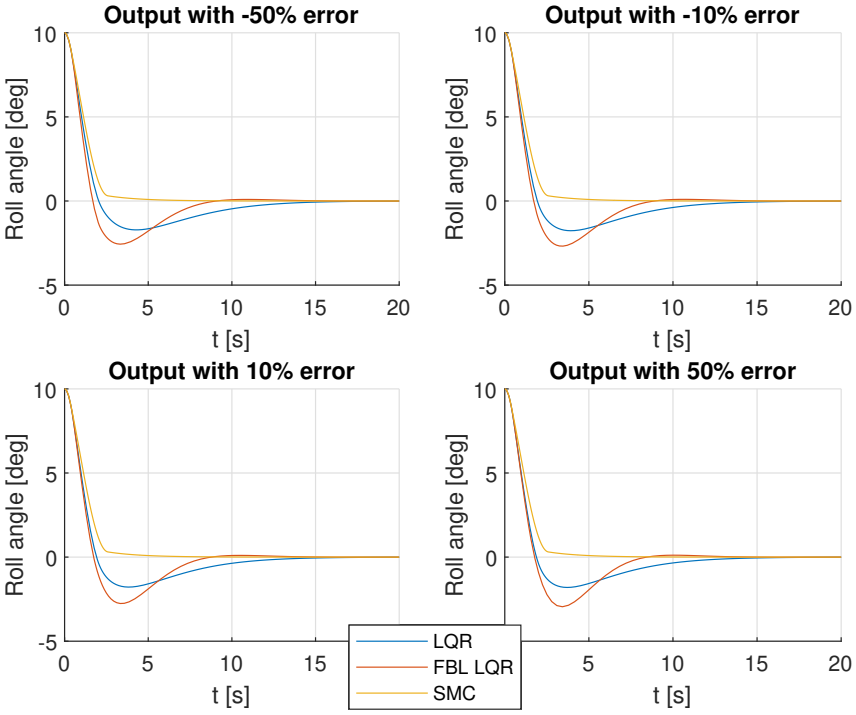

Figure 4.2: System output with uncertainty, no waves

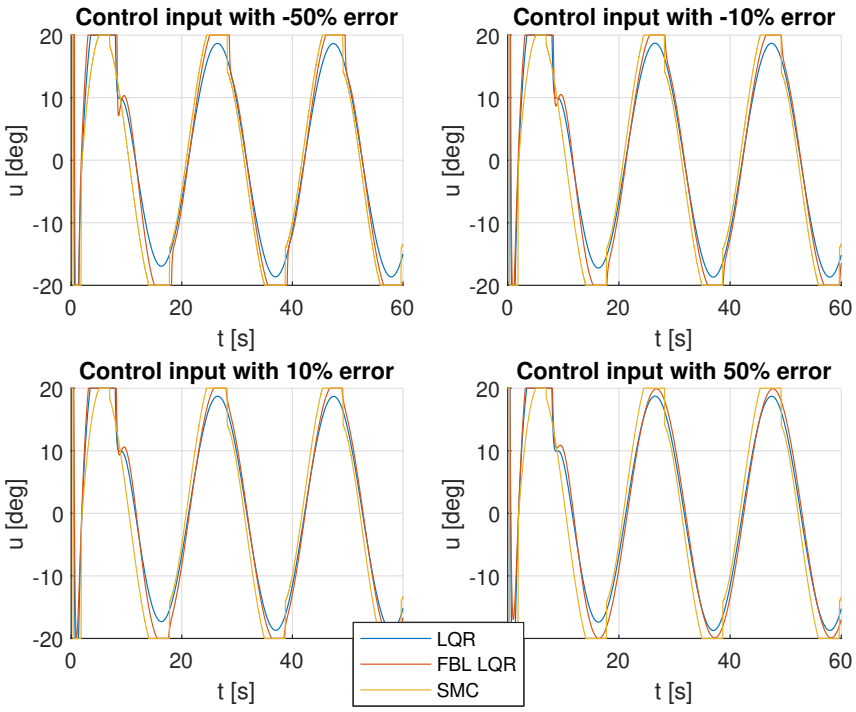

Figure 4.3: Control input with uncertainty, $\omega_w = 0.3$

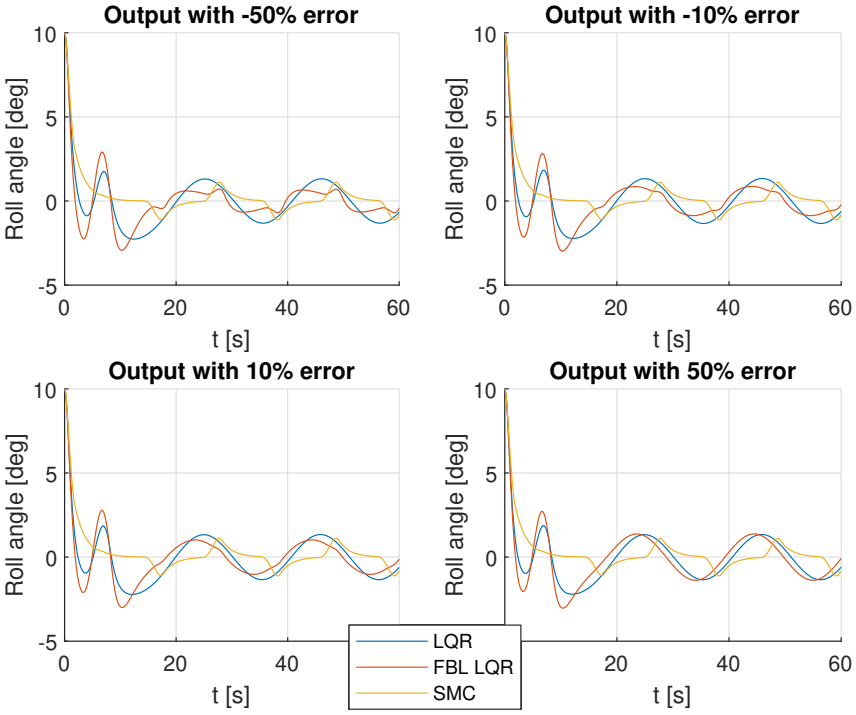

Figure 4.4: System output with uncertainty, $\omega_w = 0.3$

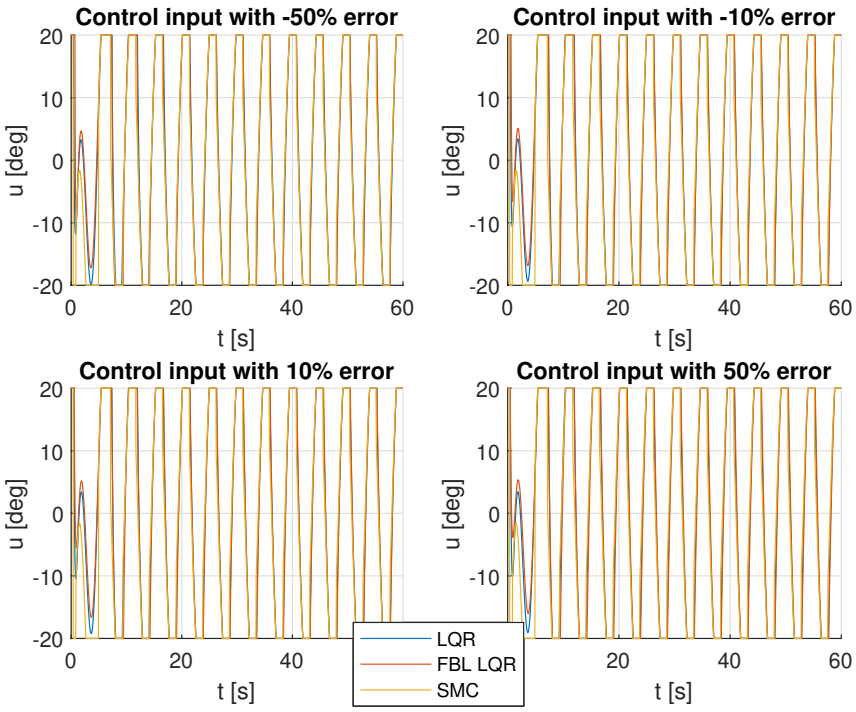

Figure 4.5: Control input with uncertainty, $\omega_w = 1.3$

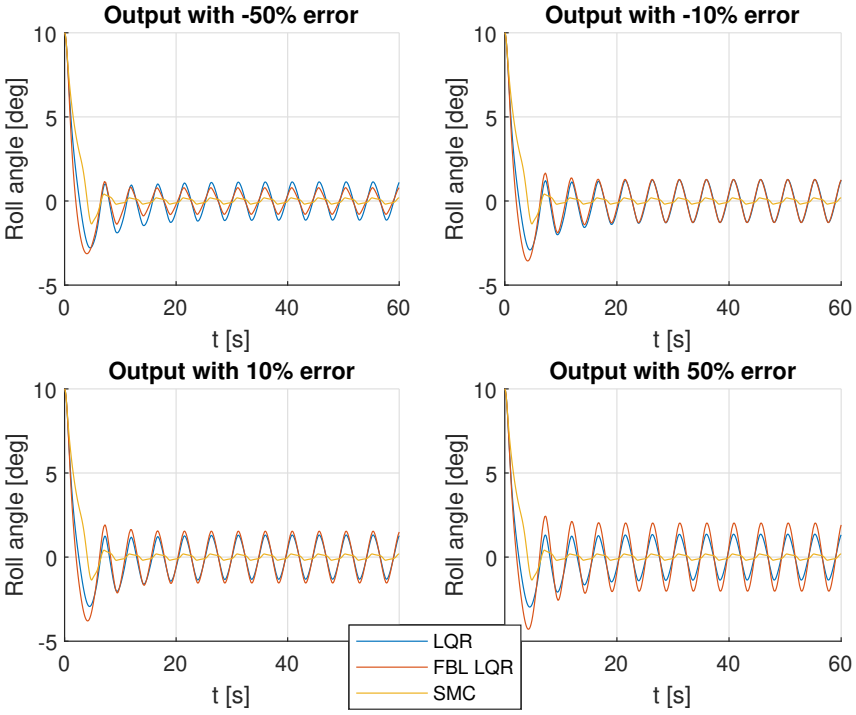

Figure 4.6: System output with uncertainty, $\omega_w = 1.3$

4.2 Controllers comparison

All three controllers developed in this project satisfy the control specifications. Since the open-loop system behaves very much like its linearization around the origin, there's no real advantage in using the LQR on the feedback linearized system compared to a standard LQR on the nonlinear system. This intuition is supported by the very similar output of the LQR controller on the linearized and nonlinear systems, as shown in Figure 3.4, and is confirmed by the similar results between the two controllers shown in Table 4.3. However, the best performance is achieved using the Sliding Mode Controller, which provides a very low settling time and excellent disturbance rejection properties. It also excels in maintaining consistent performance across a wide range of parametric errors, as shown in Table 4.1 and Table 4.2. The downside of SMC is that it requires higher effort from the actuators, even in the absence of disturbance. If the actuators cannot perform such control actions, the actual performance on the physical system will be significantly degraded.

Error (%)	LQR Ts [s]	FBL Ts [s]	SMC Ts [s]
-50	7.46	6.17	2.08
-10	7.08	6.19	2.08
10	6.99	6.19	2.08
50	6.88	6.15	2.08

Table 4.1: Settling time with different values of error ε

Error (%)	ω_w	LQR Amplitude [deg]	FBL Amplitude [deg]	SMC Amplitude [deg]
-50	0.3	1.3176	0.6945	1.1159
-10	0.3	1.3362	0.8687	1.1158
10	0.3	1.3406	1.0231	1.1156
50	0.3	1.3455	1.3779	1.1155
-50	1.3	1.1355	0.7906	0.1862
-10	1.3	1.2748	1.2850	0.1856
10	1.3	1.3130	1.5411	0.1864
50	1.3	1.3638	2.0205	0.1864

Table 4.2: Output amplitude after the transient with different values of error ε

Controller	Parameter	$\omega = 0.3$	$\omega = 1.3$
Uncontrolled	Amplitude	6.65	7.34
	Ts (10 deg - 1 deg)	35.7s	
LQR	Amplitude	1.34	1.29
	Reduction	-79.85%	-82.43%
	Ts (10 deg - 1 deg)	6.89s	
FBL + LQR	Amplitude	0.94	1.43
	Reduction	-85.86%	-80.52%
	Ts (10 deg - 1 deg)	6.24s	
SMC	Amplitude	0.91	0.60
	Reduction	-86.32%	-91.83%
	Ts (10 deg - 1 deg)	2.08s	

Table 4.3: Summary of controller results on nominal parameters

Chapter 5

Conclusions and further developments

In this project, we analyzed a nonlinear dynamical system representing the 1-DOF roll motion of a vessel at sea and developed both linear and nonlinear controllers to maintain the ship in an upright position and dampen oscillations caused by wave disturbances.

The open-loop analysis revealed that, despite numerous equilibrium points appearing far from normal operating values and many bifurcations occurring when parameters lose physical meaning, the system origin is asymptotically stable with a large region of attraction. It is also structurally stable when parameters vary in a physically meaningful way. This indicates that the controlled system does not require particular attention due to unstable equilibria or bifurcations. All controllers achieved very good results. SMC demonstrated its advantages when there are demanding specifications for disturbance rejection and robustness.

It is important to note that this model is an oversimplified representation of ship dynamics and cannot be directly applied to a real fin stabilizer system. However, it provides insights into how nonlinear control strategies can achieve these goals. An immediate further development would be to include actuator dynamics in the model, as this is a primary constraint when dealing with real physical systems. The Sliding Mode Controller outperformed LQR and FBL; however, the required control action is very fast, and if the actuators are not able to achieve such performance, the effectiveness of the control degrades rapidly. Additionally, using a 6-DOF dynamic model that accounts for coupling dynamics would increase the complexity of the controllers but is a necessary step before implementing such a controller on a real vessel.

Bibliography

[1] Rolls-Royce. *Rolls-Royce new stabiliser range offers greater stability for ice class ships*. 2023. URL: https://www.rolls-royce.com/media/press-releases/2018/09-08-2018-rr-new-stabiliser-range-offers-greater-stability-for-ice-class-ships.aspx (visited on 12/23/2023).

[2] Taher Awad, Mohamed Abd-elfatah Elgohary, and Tawfik Elemam Mohamed. "Ship roll damping via direct inverse neural network control system". In: *Alexandria Engineering Journal* 57.4 (2018), pp. 2951–2960. ISSN: 1110-0168. DOI: https://doi.org/10.1016/j.aej.2018.06.001. URL: https://www.sciencedirect.com/science/article/pii/S1110016818300930.

[3] Henk Nijmeijer. "Control of nonlinear mechanical systems". In: Mar. 2002, pp. 79–79. ISBN: 0-7803-7270-0. DOI: 10.1109/IDC.2002.995381.

[4] Tristan Perez and Mogens Blanke. "Ship roll damping control". In: *Annual Reviews in Control* 36.1 (2012), pp. 129–147. ISSN: 1367-5788. DOI: https://doi.org/10.1016/j.arcontrol.2012.03.010. URL: https://www.sciencedirect.com/science/article/pii/S1367578812000119.

[5] A. Dhooge, W. Govaerts, and Yu. A. Kuznetsov. "MATCONT: A MATLAB package for numerical bifurcation analysis of ODEs". In: *ACM Trans. Math. Softw.* 29.2 (June 2003), pp. 141–164. ISSN: 0098-3500. DOI: 10.1145/779359.779362. URL: https://doi.org/10.1145/779359.779362.